Multi-scale and -contrast sensorless adaptive optics optical coherence tomography

Myeong Jin Ju[1,2], Destiny Hsu[1], Ji Hoon Kwon[1], Daniel J. Wahl[1], Stefano Bonora[3], Yifan Jian[4], Shuichi Makita[5], Yoshiaki Yasuno[5], Marinko V. Sarunic[1]

[1]Department of Engineering Science, Simon Fraser University, Burnaby, Canada; [2]Beckman Laser Institute-Korea, College of Medicine, Dankook University, Cheonan, South Korea; [3]CNR-Institute for Photonics and Nanotechnology, Padova, Italy; [4]Casey Eye Institute, Oregon Health & Science University, Portland, Oregon, USA; [5]Computational Optics Group, University of Tsukuba, Tsukuba, Ibaraki, Japan

Correspondence to: Marinko V. Sarunic. Department of Engineering Science, Simon Fraser University, Burnaby, Canada. Email: msarunic@sfu.ca.

Background: The roles of the retinal microvasculature and the retinal pigment epithelium (RPE) in maintaining the health and metabolic activity of the retina lend great clinical value to their high-resolution visualization.

Methods: By integrating polarization diversity detection (PDD) into multi-scale and -contrast sensorless adaptive optics optical coherence tomography (MSC-SAO-OCT), we have developed a novel multi-contrast SAO OCT system for imaging pigment in the RPE as well as flow in the retinal capillaries using OCT angiography (OCTA). Aberration correction was performed based on the image quality using transmissive deformable optical elements.

Results: MSC-SAO-OCTA imaging was performed at multiple fields-of-view (FOVs) with adjustable numerical aperture (NA). Retinal flow and RPE structural images for *in vivo* healthy and pathological human posterior eyes were demonstrated to show clinical feasibility of the system.

Conclusions: High-resolution imaging of retinal vasculature at both large and small FOVs, as well as characterization of RPE topology and deformation, enables more sophisticated and concise investigation of retinal pathologies for *in vivo* human imaging. MSC imaging may permit detection and analysis of even subtle deformations in the RPE layer using a single instrument.

Keywords: Optical coherence tomography (OCT); adaptive optics; angiography; polarimetric imaging; retina; ophthalmology

Introduction

The structure of retinal vasculature is hierarchical, comprised of multiple layers of capillary networks. The networks are commonly divided into the superficial capillary plexus and the deep capillary plexus (1). These vasculature layers supply the inner retina with oxygen and important nutrients, as well as remove by-products of retinal metabolism. In contrast, the outer retina is supplied by the choroid. The retinal pigment epithelium (RPE) is a single layer of cells immediately adjacent to the choriocapillaris,

and provides metabolic regulation for the photoreceptor layer (2,3). The effects of common retinal vascular diseases are variable due to the specific nature and locality of the insult, spanning vascular defects (blockage of blood flow, leakage of fluid, or ruptured vessels) to disturbances in RPE structure (such as RPE atrophy and detachment), all of which can be characteristic of pathologies leading to loss or impairment of vision, including diabetic retinopathy (DR), age-related macular degeneration (AMD), and pigment epithelial detachment (PED) (4,5). Direct visualization and segmentation of both retinal vasculature and RPE would

therefore be of considerable diagnostic value.

Optical coherence tomography (OCT), a non-invasive imaging modality used to obtain high resolution volumetric images of the retina, has become an essential tool for detecting and investigating retinal diseases (6-8). The clinical utility of OCT for diagnosis has been further extended by development of OCT-based angiography (OCTA). By measuring variations of OCT signals caused by moving cells, OCTA allows examination of blood flow contrast and the hierarchal structure of retinal vasculature without the need for contrast agents (9-16). Another form of contrast in OCT is based on detecting the changes in polarization, called polarization sensitive OCT (17). Recently, Makita *et al.* (18) have reported an advancement in OCT imaging systems called a pigment-and-flow OCT (PAF-OCT), capable of generating degree of polarization uniformity (DOPU) contrast by measuring randomness of polarization (RP) as well as OCTA. The PAF-OCT system is able to be implemented with minimal extension to a standard swept-source based OCT system; the principle additional hardware for PAF-OCT is a polarization diversity detection (PDD) unit that is originally utilized for Jones matrix OCT (JM-OCT) (19). Unlike JM-OCT, PAF-OCT uses a single input polarization probe beam to calculate the RP with the noise-corrected DOPU algorithm (20). Using the PAF-OCT system, structural, pigment, and vasculature imaging were simultaneously performed on normal and pathological subjects, which showed great potential for application in an ophthalmic clinic.

In this manuscript, we introduce an upgraded version of the original PAF-OCT system that can perform multi-scale and -contrast OCT imaging, along with integrated sensorless adaptive optics (SAO). Through the addition of a zoomable collimator and the use of larger diameter lenses in the sample arm, the multi-scale and -contrast SAO-OCT (MSC-SAO-OCT) system permitted a dynamic probing beam diameter that is adjustable to accommodate narrow to wide fields-of-view (FOVs) with minimal impact on imaging protocols, allowing expeditious multi-scale data acquisition within a single imaging session. With the introduction of transmissive adaptive elements, which can be easily integrated into existing OCT systems, SAO can be applied to compensate for ocular aberrations at higher numerical apertures (NAs), improving resolution of retinal structures at low cost and in a small design footprint (21,22). *In vivo* human retinal images from healthy and pathological subjects were taken to validate MSC-SAO-OCT and demonstrate clinical utility.

Methods

Figure 1 shows a schematic of the MSC-SAO-OCT, based on our previously reported lens-based SAO-OCT system (21). A swept laser (Axsun Technologies Inc., Billerica, MA, USA) with a 100 kHz wavelength sweep rate, a duty cycle of 60%, a center wavelength of 1.06 μm and a full width at half maximum (FWHM) of 85 nm was used as a light source. There are two interferometers, a phase calibration unit and OCT interferometer. The source output was split by a 20:80 single-mode fiber coupler. The 20% port of the fiber coupler was connected to a 50:50 fiber coupler, with one port directed to the calibration unit and the other to the OCT reference arm. The 80% portion of source light was directed to a 50:50 fiber coupler; one port was directed to the calibration unit and the other to the OCT sample arm. In the phase calibration unit, a desired optical path difference was set by moving one of the mirrors. As shown in the diagram of FFT signals (inset of *Figure 1*), the phase calibration signal (green) appeared at a depth close to DC without overlapping the DC (black) or OCT signals (blue). In order to avoid any interference between the OCT and calibration signals, ~1.5 m fiber patch cables were added into the OCT interferometer. In the OCT reference arm, a dispersion compensation block was inserted to match the dispersion of the sample arm. The OCT sample arm consisted of a zoomable fiber collimator (ZFC; ZC618APC-B, Thorlabs Inc., Newton, NJ, USA), multi-actuator adaptive lens (MAL; research prototype designed by Dr. Stefano Bonora, CNR-Institute for Photonics and Nanotechnology, Padova, Italy) (22,23), variable focus lens (VFL; ARCTIC 39N0, Corning Varioptic Lenses, Corning, NY, USA), achromatic doublet lenses, and a 2D galvanometer scanner (GS) to deliver a scanning beam to the pupil of the subject. The OCT and phase calibration signals were detected by the PDD unit that consisted of a non-polarization-sensitive beam splitter, two polarizing beam splitters, and two balanced photodetectors (PDB471C, Thorlabs Inc., Newton, NJ, USA). The non-polarization-sensitive beam splitter served to combine the reference and sample backscattered light, with the polarization state of the reference light controlled with a linear polarizer, oriented at 45° to produce two equally distributed orthogonal polarization states (18). The two orthogonally polarized interference signals were digitized by a digitizer (ATS9350, Alazar Technologies Inc., Pointe-Claire, QC, Canada) with
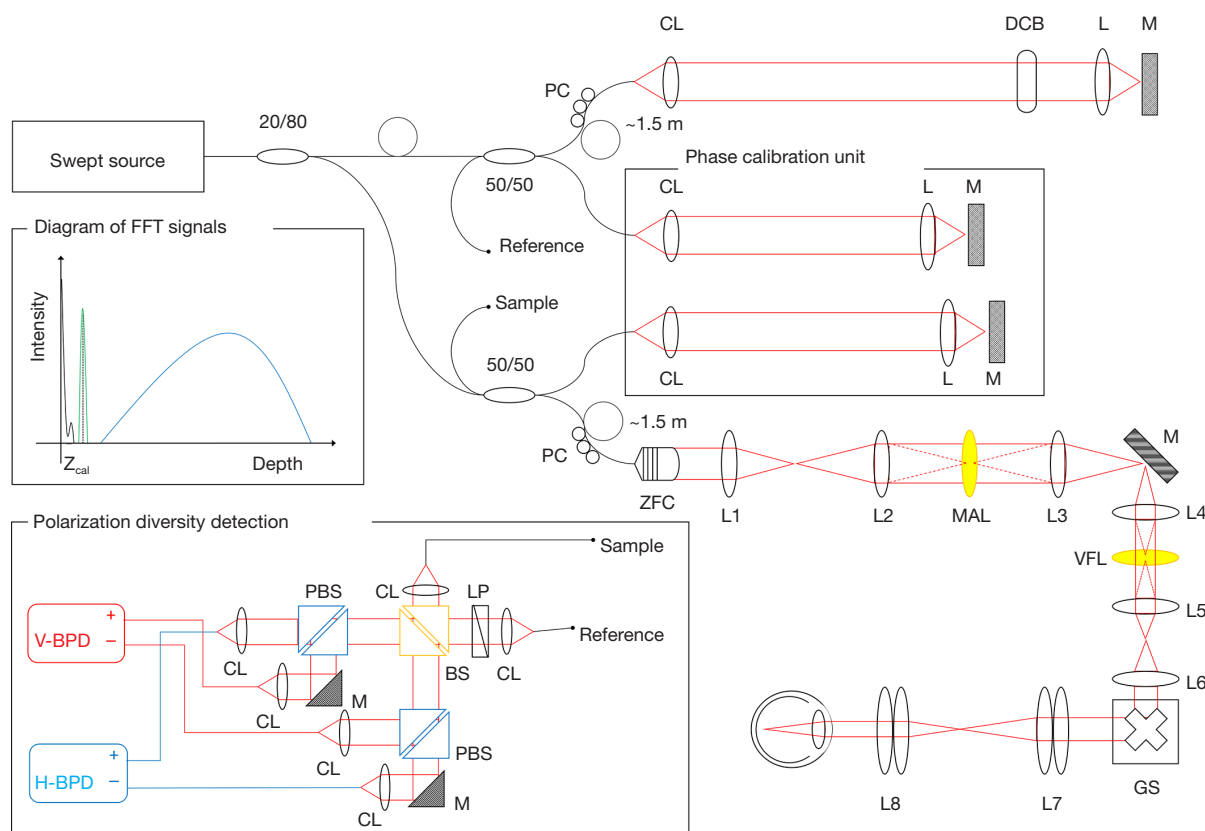
Figure 1 Schematic of MSC-SAO-OCT system. Zoomable fiber collimator (ZFC); multi-actuator adaptive lens (MAL); variable focus lens (VFL); polarization controller (PC); collimation lens (CL); lens (L); mirror (M); dispersion compensation block (DCB); 2D galvanometer scanner (GS); vertical- & horizontal balance photodetector (V- & H-BPD); beam splitter (BS); linear polarizer (LP); polarization beam splitter (PBS); {L1, L2, L3, L4, L5, L6, L7, L8} = {50, 100, 200, 75, 50, 60, 75, 50} mm.

12-bit resolution and a sampling rate of 500 MHz.

To achieve a phase-resolved OCT signal, the spectral shift caused by fluctuation in the synchronization between the wavelength sweep of the source and the digitization was estimated and corrected by the phase stabilization algorithm described in the appendix of Ref. (24). The scanning property of the light source, the parameters for the sampling of the spectral interference signal, and the windowing finally defined the measured depth-resolution of 10.5 μm in air, corresponding to ~7.6 μm in tissue (n=1.38). With an average probe power of 1 mW, the sensitivity was measured to be ~90 dB, and the signal roll-off, measured at a depth range of 0.3 to 2.5 mm, was ~–1 dB/mm. Since the signal energy is split into two OCT images due to PDD, the sensitivity of the system, when measured for a single image, is 3 dB lower than that of standard OCT. By accounting for the fundamental loss from the 50:50 fiber coupler, the shot-noise-limited sensitivity of a single-channel image becomes

~101 dB. The departure of the measured sensitivity from the shot-noise-limited sensitivity by –12 dB is accounted for by the round-trip optical loss of the scanning head (including the MAL and VFL), which has been measured to be –8 dB, the fiber coupling loss at the detection, measured to be –3 dB, and a recoupling loss of –1 dB from the misalignment of a mirror sample for sensitivity measurement.

In this system, three different NA imaging modes can be set via adjusting the ZFC: low, middle and high NAs with a nominally 1, 2, 3 mm beam diameter at the cornea, respectively, based on the $1/e^2$ beam diameters at the focal plane in front of the collimator as reported by the manufacturer and following propagation through the lens elements of the system. Assuming a 22.2 mm focal length of the eye and refractive index of 1.33 for water at 1.06 μm, the transverse resolutions defined by $\Delta x_{OCT} = 0.51\lambda/NA$ (25) were estimated to be 18.05, 9.02 and 6.02 μm with low (0.03), middle (0.06) and high (0.09) NAs, respectively. The axial

position of the focal plane of the probe beam was guided to specific retinal layers by adjusting the VFL for bulk defocus compensation. The MAL was used for aberration correction as well as for fining tuning of the defocus (21,23,26). With a pupil diameter of 3 mm, approximately 90% of the aberrations in the human eye are accounted for Zernike modes up to the 2nd radial order (27), therefore the aberration correction with the MAL was restricted to defocus and two astigmatisms and only employed when imaging with the highest NA.

Using the two orthogonally-polarized OCT volumes detected by PDD, RP information was calculated based on the DOPU algorithm presented in Ref. (20), producing data selectively visualizing the RPE layer due to its intrinsic polarization scrambling properties (2). An RPE elevation map was created based on DOPU contrast, serving as the backdrop for MSC *en face* images (28). Computation of retinal vasculature flow information was provided following coherent summation of the two orthogonal polarization detection channels and estimation of the complex temporal variance of the signal across repeated B-scans (24). The retinal angiography and RPE topology were combined to form the final MSC image sets.

At an initial wide FOV imaging mode with a low NA setting, a transverse area of 9 mm × 9 mm was scanned with 1,000 A-lines × 1,000 B-scans for general morphological observation of the retina with OCT and DOPU contrast, which permits cursory identification of regions-of-interest (ROIs). Subsequently, zoomed volumes of the ROIs were scanned with 500 A-lines × 500 B-scans with 4 repeated scans (BM-scans) in a single transverse location, at middle and high NAs for FOVs of 6 mm × 6 mm and 3 mm × 3 mm, respectively. In the imaging protocol for middle and high NAs, the BM-scans were used to generate high-resolution MSC images with comprehensive structural and flow contrast to facilitate identification of retinal pathologies. Each of the imaging protocols required 10 s for acquisition with the 100 kHz source; the acquisition time can be reduced by using a faster swept laser. For example, a source with a 400 kHz A-scan rate (already commercially available) would reduce the imaging time to 2.5 s. Imaging was performed using a modified version of the real time acquisition and display software permitting simultaneous view of B-scans from both polarization channels, as well as OCTA (29-31). A fixation target, head strap, and chin rest were utilized to minimize motion during acquisition with subjects trained in fixation. Human imaging was performed with approval from the Office for Research Ethics at Simon Fraser University. Written, informed consent was obtained prior to imaging.

Figure 2 presents a visual representation of the stages within the MSC-SAO-OCT image processing pipeline. Following acquisition of the volumetric OCT data, the intensity of the OCT signal was first calculated by summation of the OCT signal powers of the two polarization channels to create polarization-independent scattering contrast (20). For the cases of repeated B-scans at a single transverse location, the so called BM-scans were averaged temporally across the frames. Generation of the blood flow contrast was performed on the coherent summation of the two orthogonally-polarized volumes through computation of the temporal complex variance of the OCT signal, estimated as described in Ref. (24). For polarization contrast processing, DOPU contrast was generated for visualization of the RPE layer through quantification of the RP from the two PDD-detected OCT signals via application of the DOPU algorithm (20), permitting simple segmentation and depth localization of the layer by thresholding. The DOPU cross-sections were visualized with a rainbow colourmap, with values of DOPU ranging from zero to one mapped to colours from blue to red. To visualize the retinal structures with DOPU contrast, final images for display were composed by multiplying the DOPU image against the log-scaled intensity OCT in the same transverse location (18).

Retinal flow contrast for middle and small FOVs was generated through automated segmentation of the OCTA transverse scans, averaging along the depth between the inner limiting membrane (ILM) and outer plexiform layers (OPL) (24). For wide FOV, the size of the data and time required for acquisition rendered multiple B-scans per volume impractical for *in vivo* human imaging. A map of the relative change in RPE elevation across the FOV was developed based on the methods described in Ref. (32). Each transverse DOPU scan was searched along their depth, with the depth index of DOPU values below the threshold value of 0.95 extracted for every A-scan. Of these indexes, the median value was taken as the centroid of the RPE layer, and the collected values displayed using a jet colourmap, scaled to display their relative elevations.

Results

Figures 3 and *4* illustrate MSC-SAO-OCT image processing with representative image results for middle and small FOV, and wide FOV, respectively. MSC images concentrated
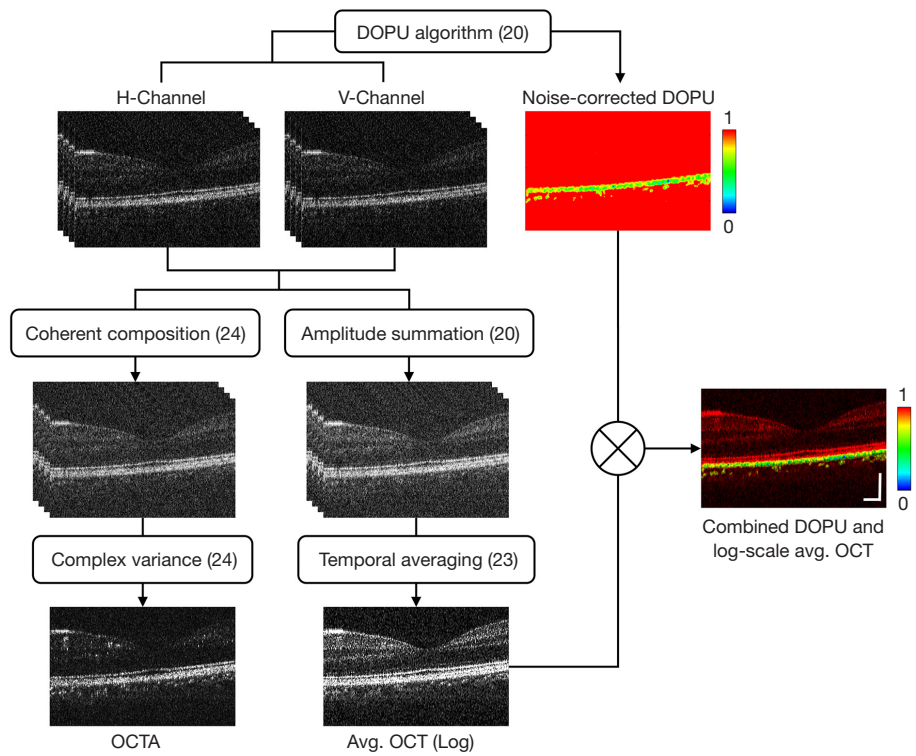
Figure 2 Pipeline for MSC-SAO-OCT image processing (20,23,24). Sample dataset was taken at a 3 mm × 3 mm FOV with four repeated B-scans at the same transverse location. The scale bar indicates 250 μm.
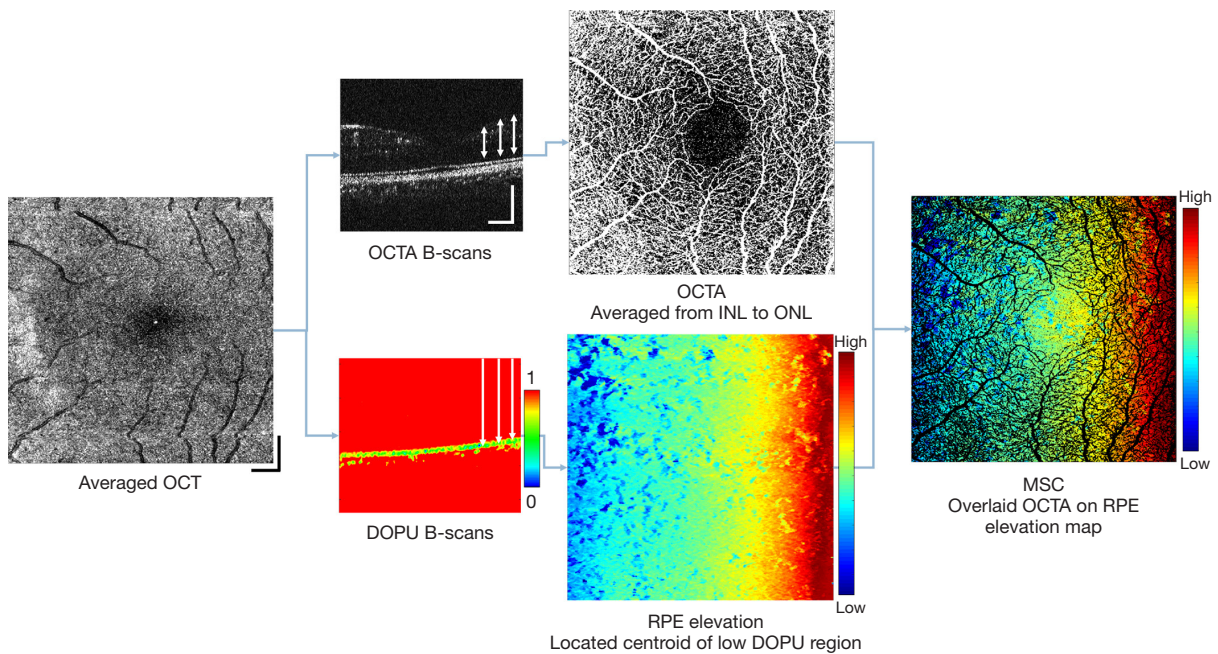

Figure 3 Schematic of MSC-SAO-OCT image processing for middle and small FOV imaging protocols. Sample dataset was taken at a 3 mm × 3 mm FOV with four BM-scans. OCTA B-scans were averaged from the INL to the ONL, as indicated by the double-ended arrows to produce the *en face*. The centroid of the low DOPU region was found for each A-scan, as indicated by the single-ended arrows in the B-scan, to produce the RPE elevation map. MSC images then combined the two *en face* projections. The scale bar indicates 250 μm.
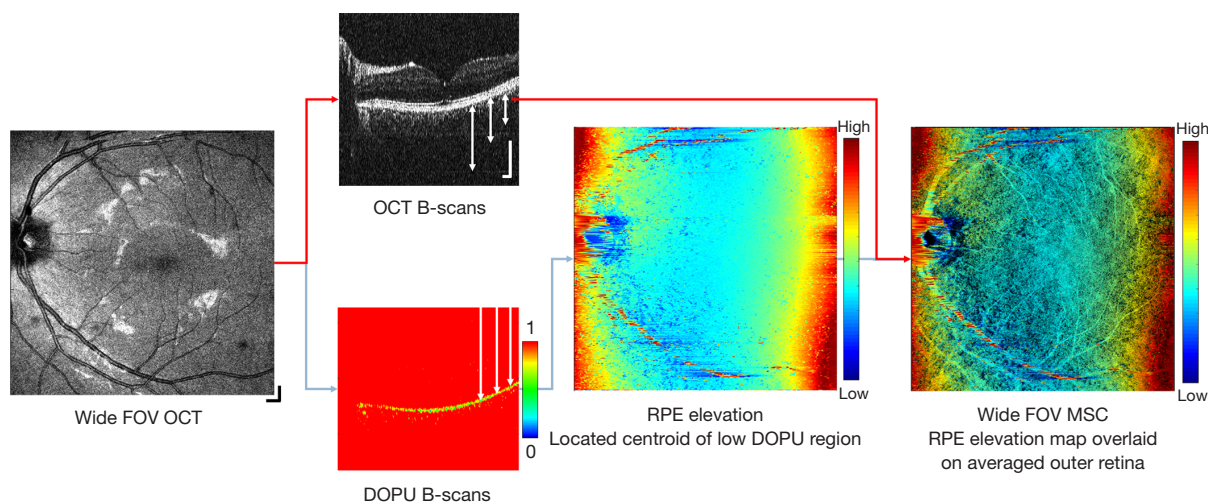
Quant Imaging Med Surg 2019;9(5):757-768 | http://dx.doi.org/10.21037/qims.2019.05.17

Figure 4 Schematic of MSC-SAO-OCT image processing and composition for wide FOV imaging protocol. Sample dataset was taken at a 9 mm × 9 mm FOV. OCT B-scans were averaged across the outer retina, as indicated by the double-ended arrows. The centroid of the low DOPU region was found for each A-scan, as indicated by the single-ended arrows in the B-scan, to produce the RPE elevation map. MSC images then combined the two *en face* projections. The scale bar indicates 250 µm.

on observation of inner retinal structures were generated by superimposing the retinal vasculature images (vessels in black) over the RPE elevation map, integrating the blood flow signal data contributed by OCTA imaging with topological RPE layer information conferred via DOPU contrast, while wide FOV MSC images concentrated on outer retinal structures. RPE elevation maps were generated as relative measurements, the highest points of the RPE in the volume mapped to red and the lowest points to blue, with the curvature and any disturbances in the layer structure exhibiting a gradient between the two values.

Figure 5 shows a representative image set acquired from the left eye of one healthy subject, displaying all the modalities available for a single imaging session, with NAs selected to maximize the transverse resolution at each FOV for the given scanning protocols. An *en face* scattering intensity image with low NA is displayed in *Figure 5A*, spanning from the macula region to the optic nerve head (ONH). *Figure 5B,C,D* present macular MSC images (center) ranging from low, middle, to high NA, respectively, with their respective wavefront aberration correction applied via VFL and MAL (top), and DOPU B-scans extracted from the cross-section across the retinal structures at the location of the dotted lines (bottom). In the presence of melanin, DOPU values are lower relative to surrounding tissues (2), with the resulting B-scan exhibiting selective tissue contrast at the RPE layer and parts of the

choroid. The extent of the region visualized in each *en face* is indicated by the green, red, and blue borders in *Figure 5A*. In *Figure 5B*, general outer retinal structures are visible beneath the RPE layer, while in *Figure 5C,D* the full hierarchy of the retinal vasculature network is visible encircling the fovea, from the superficial vessels to the deep capillaries of the OPL. The RPE topology is indicative of a healthy eye, displaying a subtle but continuous gradient due to the curvature of the retinal surface, further supported by the DOPU B-scans showing a smooth and continuous melanin layer.

The MSC imaging modalities were also applied to a case exhibiting mild foveal drusen. *Figure 6* presents the results in a demonstrative image set analogous to those displayed in *Figure 5*. The scattering intensity *en face* image in *Figure 6A* shows a region of abnormally low signal magnitude at the fovea, with the cross-sectional DOPU contrast image of *Figure 6B* at the same FOV detecting a detachment of the RPE at the corresponding location. Further zoomed-in FOV volumes centered around the macula in *Figure 6B,C,D* present MSC images (center) with point discolourations and DOPU cross-sections (bottom) with RPE detachments collocated at the aberrant region in *Figure 6A*, with the location of the drusen indicated by the white arrows in each image. While the slight elevation of the drusen were difficult to observe relative to the natural curvature of the retina at a wide FOV, with multi-scale
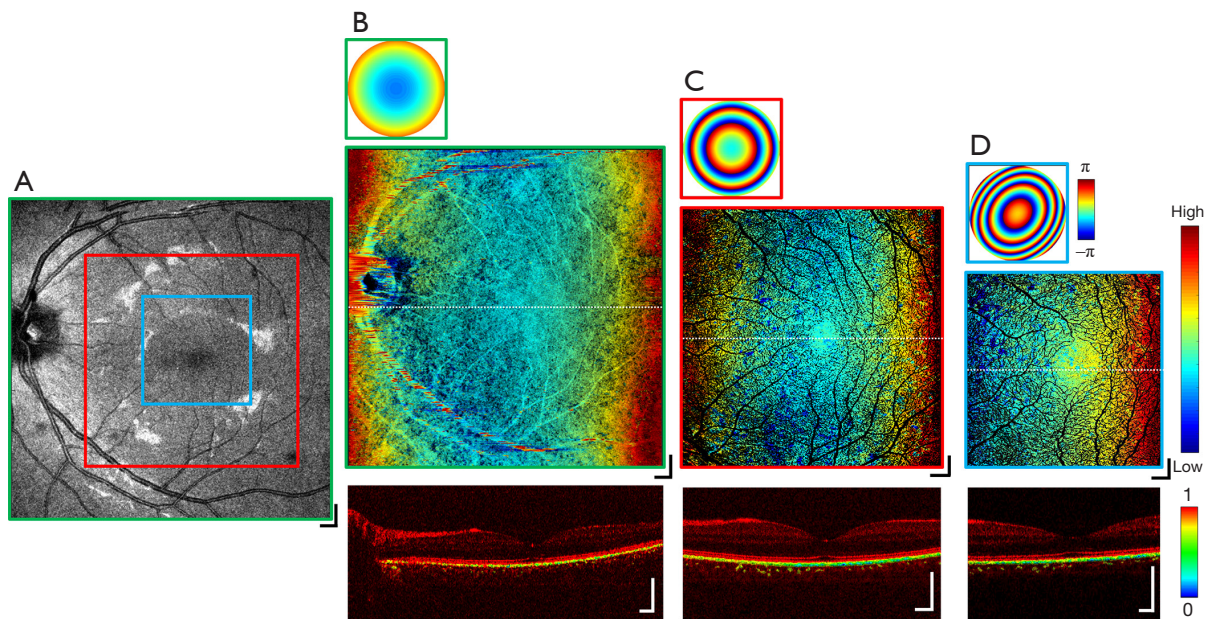
Figure 5 Representative image set from a healthy subject. (A) Fundus *en face* of retina spanning from ONH to fovea with 9 mm × 9 mm FOV. Green, red, and blue boundaries indicate areas visualized by (B-D) respectively. (B-D) Wavefront compensation applied at the given NA (top), *en face* MSC images centered about the fovea (center) and DOPU B-scans taken from the white line (bottom) with 9 mm × 9 mm, 6 mm × 6 mm FOV and 3 mm × 3 mm FOV respectively. The scale bar indicates 250 μm.
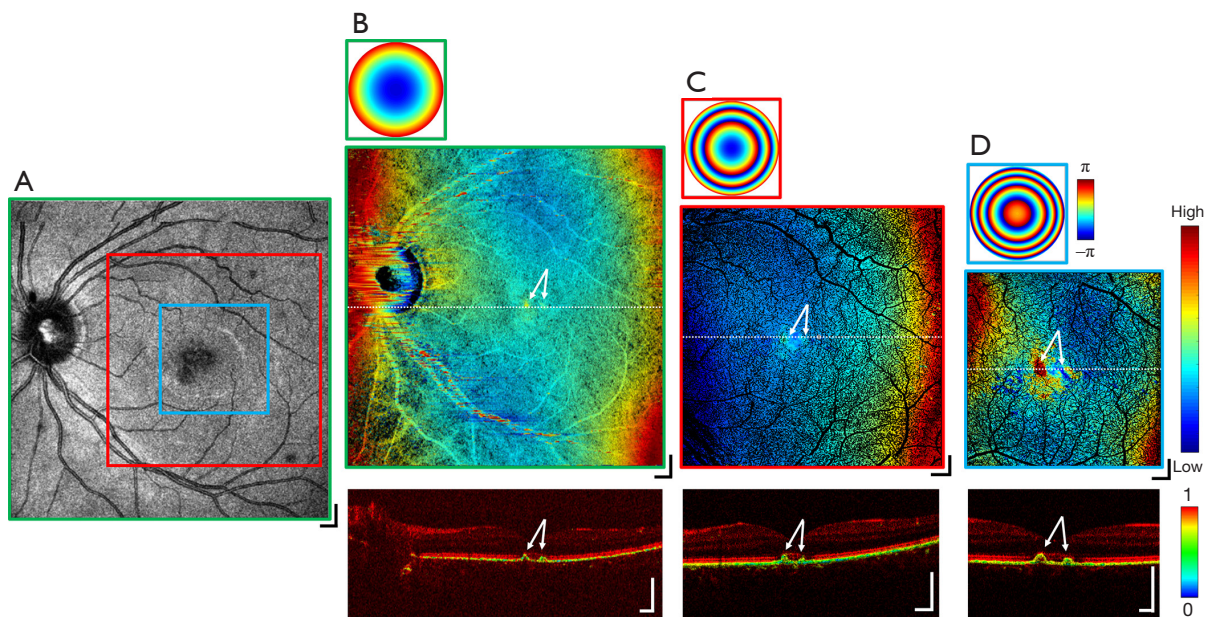

Figure 6 Imaging results from subject with drusen. (A) Fundus *en face* of retina spanning from ONH to fovea with 9 mm × 9 mm FOV. Green, red, and blue boundaries indicate areas visualized by (B-D) respectively. (B-D) Wavefront compensation applied at the given NA (top), *en face* MSC images centered about the fovea (center) and DOPU B-scans taken from the white line (bottom) with 9 mm × 9 mm, 6 mm × 6 mm FOV and 3 mm × 3 mm FOV respectively. The arrows indicate the location of the drusen in each image. The scale bar indicates 250 μm.

imaging, the shape of the drusen was pronounced within the zoomed-in images. The height of the drusen relative to the surrounding RPE was indicated by the focal hot spots in their respective MSC *en face* images, whereas visualization in the DOPU contrast B-scans revealed changes in the RPE elevation but not regions of atrophy. Although not demonstrated here, this may be useful in future studies to display the extent of choroidal neovascularisation in wet AMD and geographic atrophy in dry AMD.

Discussion

DOPU evaluation with multi-scale imaging

Building on previous PAF-OCT systems reported in Ref. (18) to integrate multi-scale imaging, the MSC-SAO-OCT system described in this report acquires images at a range of NAs through adjustment of the probing beam diameter. This variation in the beam diameter permits the matching of lateral resolution to the desired FOV without the need for drastic amendments to the scanning protocols.

Increasing the imaging NA results in a shorter imaging depth range due to the restricted width of the focal waist. In this study, MSC imaging was focused on inner retinal structures at smaller FOVs (*Figures 5D,6D*) for the best visualization of the OPL, and thus the RPE risked becoming out of focus, compromising the integrity of calculated DOPU values. However, the depth of focus (DOF) of our system, with a maximum transverse resolution of 6.02 µm, was determined to be around 215 µm according to $DOF_{ZOCT} = 2\pi \Delta x_{OCT}^2/\lambda$ (25), adequate to cover the depth range from ILM to RPE. In order to validate our method, investigation of the effect of changing focal plane on DOPU measurements was performed by taking consecutive high NA volumes at the same location on the retina, with the focus moved between the inner to the outer retinal layers, presented in *Figure 7*. From the intensity scattering OCT cross-sections in *Figure 7A*, although the inner retinal layers appear more pronounced in the OPL-focused volume, no significant sharpness change can be observed between the two volumes at the RPE. When observing the DOPU cross-sections (*Figure 7B*) and the *en face* DOPU projections averaged along the RPE depth (*Figure 7C*), both volumes exhibit consistently lowered values at the RPE. The volume with the focus directed at the RPE layer in *Figure 7B* displays faintly bluer colouration at the white arrows than that focused at the OPL, indicating points of lower DOPU values at equivalent locations, but which could potentially

be due equally to either movement or signal noise fluctuations rather than to the focus of the directed beam.

When computing the histograms for the calculated DOPU values extracted from the RPE of these two volumes (*Figure 7D,E*), the mean DOPU for the RPE-focused data was only marginally lower as opposed to that of the OPL-focused data. Additionally, between the two normalized histograms, there is near-negligible Euclidean distance of 0.0470 and Kolmogorov–Smirnov distance of 0.0351, with the two histograms possessing strong correlation with an asymptotic P value <0.002 at the 1% significance level, indicating that the values of both volumes possess the same distribution (33). While there may be evidence of more pronounced RPE differentiation via DOPU contrast when the focal plane is directed towards the layer itself, the variation is not statistically significant. DOPU values remain lower than the surrounding retina regardless of the location of the focal plane within the macula, ensuring the reliability of MSC-SAO-OCT results. The extent and cause of the variation in DOPU quantity due to focal plane depth control are as of yet unclear, as well as variation in measured values in severe RPE pathologies such as PED, and would be points of investigation in subsequent steps of our study.

Benefits of adjustable NA

The FOVs used in this study were selected in order to conform to clinical standards. Multi-scale imaging employs three different NA settings corresponding to each of these FOVs, selected to maximize the resolution without the need for alterations to the number of samples in the scanning protocol. The effects of varying the NA on a single FOV were investigated for retinal OCTA. Three volumes are presented in *Figure 8*, acquired on a FOV of 3 mm × 3 mm while the imaging NA was varied from low (A), middle (B) to high (C). The top row presents the 2D reconstructed wavefront correction applied during image acquisition for each corresponding NA, while the middle and bottom rows display the deep capillary plexus extracted from the OCTA and OCT volumes, respectively. The focal plane was set to the OPL using the VFL, while the MAL was only employed at the highest NA for fine defocus and astigmatism compensation. Visibility of the microvasculature increased in the OCTA *en face* with increasing NA, with vessels immediately surrounding the fovea resolved only at the middle and high NAs (*Figure 8B,C*). In addition, projection artefacts from superficial layers became diminished in the OCTA as the NA was increased, demonstrating greater
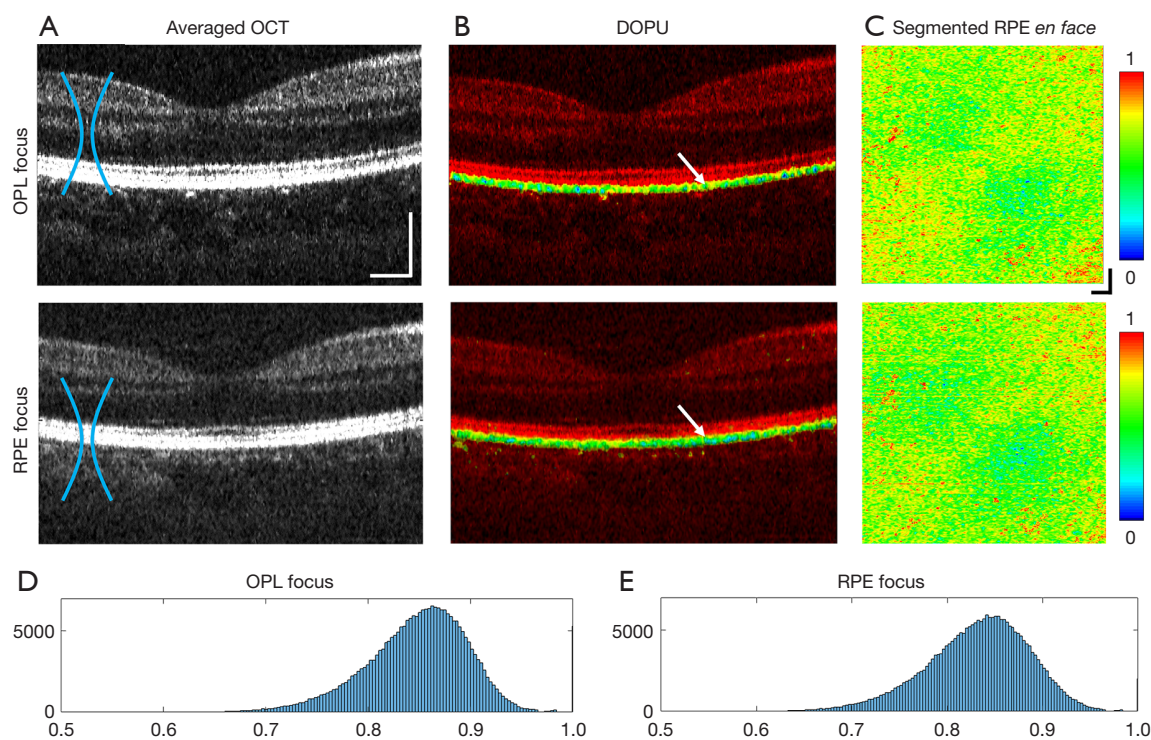
Figure 7 Comparison of imaging results from the same transverse location with the focal plane directed successively at the OPL and the RPE to test DOPU values in relation to focal plane location. (A) Averaged intensity-scattering OCT images with the location of the focal plane on the left and the DOF indicated by the blue curved line. (B) DOPU contrast cross section, with arrows indicating the same location on the RPE displaying different DOPU values, lowered in the RPE-focused volume. (C) En face projections of segmented RPE DOPU values averaged along the depth of the layer. (D,E) Histograms of DOPU values for each *en face* RPE projection. The mean DOPU values for focused scans at the OPL and the RPE were 0.8503 and 0.8330, respectively. The scale bar indicates 250 µm.

layer selectivity and clearer visualization of the deep capillary plexus.

Future development

As a pilot study to demonstrate the feasibility of MSC-SAO-OCT imaging, we demonstrated the use of MSC to selectively visualize small deformations in RPE structure at high resolution at multiple FOVs. With the layer elevation taken as a relative measurement, minute structures such as drusen are easily overlooked and overwhelmed by the general curvature of the retina, whereas in smaller FOVs they are highlighted, demonstrating the benefit of multi-scale imaging. By using the intrinsic contrast of the melanin granules in the RPE, layer segmentation can be performed without the need for computationally expensive segmentation algorithms. Reliable segmentation is essential for the localization of disturbances in the RPE, and the

use of DOPU contrast to isolate melanin concentrations is also insensitive to severe layer deformations which could induce errors in intensity-based segmentation algorithms. In order to quantify RPE elevation as an absolute measure, performing retinal curvature flattening may aid in increasing the clarity of MSC OCT images.

With this system, during real-time acquisition, MSC imaging required the OCT signal to be split into two separate V- and H-polarized channels. After processing, the two signals were recombined to match the quality of standard OCT. However, the channels were viewed individually during real-time acquisition, temporarily reducing the SNR to below that of standard OCT. The decision to use four BM-scans as opposed to two was to overcome this factor, allowing for improved quality in OCTA data and ease of real-time image acquisition. For the next steps of this study, refinement of components (such as an AR coating on the MAL) is under development,
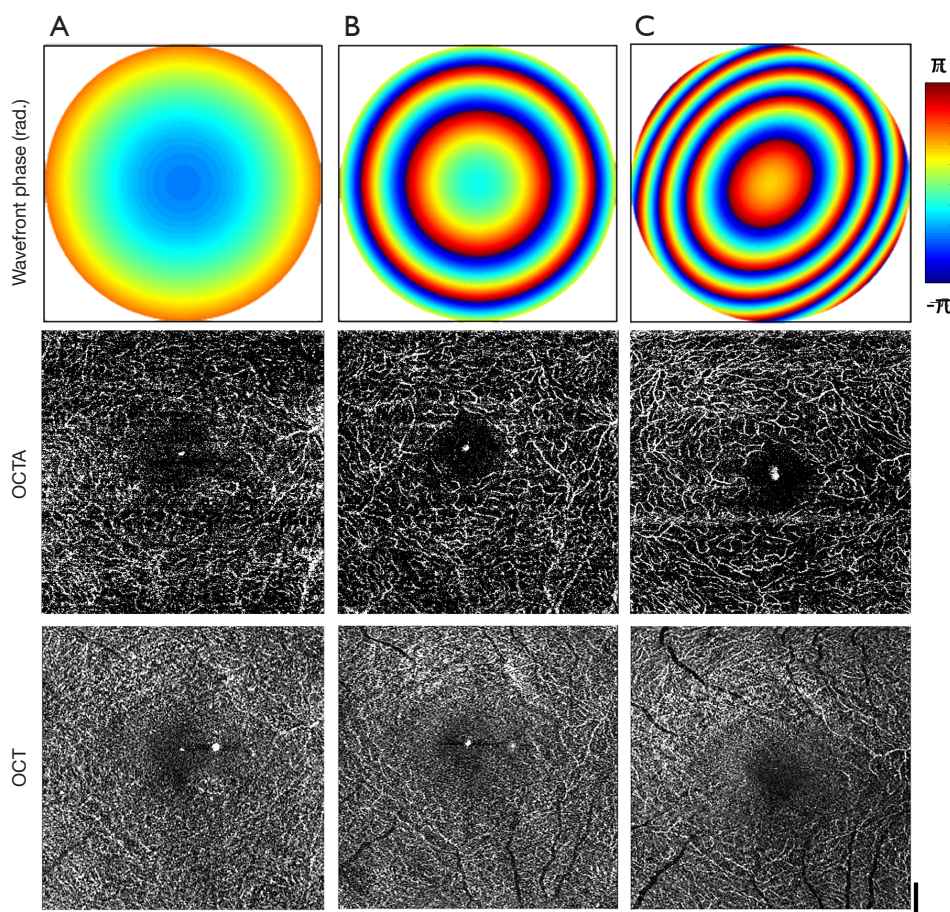
Figure 8 Deep capillary plexus images of a healthy subject centered at the fovea, with uniform FOV (3 mm × 3 mm) and varying NAs. 2D reconstructed wavefront corrections applied by SAO (top), OCTA (center) and OCT en face (bottom). From (A-C), NAs adjusted from low to high. The scale bar indicates 500 µm.

which may allow for reduced BM-scans to decrease image acquisition time without loss of quality.

A key limiting factor in regards to this proof-of-concept model was the acquisition time. The use of a 100 kHz laser governed the selection of the reported scan protocol in order to minimize acquisition time, as well as required subjects trained in fixation for minimal motion. At the lateral resolution used for each of the FOVs, the scan protocol chosen was the minimum allowable to permit feasible *in vivo* acquisition times while maintaining an adequate sampling density, and volumes were obtained demonstrating the ability to perform multi-scale high-resolution imaging, such as in *Figure 8*. In the next steps of this study, the source will be replaced with a higher speed swept laser (200 kHz, 400 kHz A-scan rates are commercially available), which will allow for reduced

scan time. For our proof-of-concept demonstration, no additional post-processing was used on the data in order to present the capabilities of the MSC-SAO-OCT system and image processing algorithm. In a clinical study, additional means of motion control can be integrated to ensure consistent acquisition of high-quality MSC images. These include introducing a motion-tracking module into the system, as well as registration and averaging of multiple serially acquired volumes (15), increasing the image SNR and overall data quality.

Conclusions

In this study, we implemented additional extensions to our previous lens-based SAO system to allow for multi-modal, multi-scale imaging with maximized resolution

at each FOV, as well as the ability to characterize both retinal vasculature and the RPE layer with inner retina MSC visualizations. These functional extensions only require minimal alterations to existing systems, while adding clinically important functionalities at a low cost (21). Furthermore, visualizing local microvasculature at both large and small FOVs, as well as characterization of RPE topology and deformation by DOPU contrast, enables more sophisticated and concise investigation of retinal pathologies for *in vivo* human imaging. MSC imaging may permit detection and analysis of even subtle deformations in the RPE layer using a single instrument. However, due to the increased acquisition time with both dual-channel imaging and SAO optimization, involuntary motion of subjects during retinal imaging will affect the quality of data. A laser with a faster A-scan rate or more robust motion-correction software is possible solutions to alleviate the issue. Therefore, future work will integrate commercially-available higher-speed light sources, in addition to considering the effectiveness of scanning protocols and software development to aid motion-free image acquisition.

Acknowledgments

Footnote

Conflicts of Interest: MJ Ju: Seymour Vision Inc. (E), Y Jian: Seymour Vision Inc. (I), MV Sarunic: Seymour Vision Inc. (I). The other authors have no conflicts of interest to declare.

References

1. Stone J, van Driel D, Valter K, Rees S, Provis J. The locations of mitochondria in mammalian photoreceptors: Relation to retinal vasculature. Brain Res 2008;1189:58-69.
2. Götzinger E, Pircher M, Geitzenauer W, Ahlers C, Baumann B, Michels S, Schmidt-Erfurth U, Hitzenberger CK. Retinal pigment epithelium segmentation by polarization sensitive optical coherence tomography. Opt Express 2008;16:16410-22.
3. Bonilha VL, Rayborn ME, Bhattacharya SK, Gu X, Crabb JS, Crabb W, Hollyfield JG. The Retinal Pigment Epithelium Apical Microvilli and Retinal Function. Adv Exp Med Biol 2006;572:519-24.
4. Ahlers C, Götzinger E, Pircher M, Golbaz I, Prager F, Schütze C, Baumann B, Hitzenberger CK, Schmidt-Erfurth U. Imaging of the retinal pigment epithelium in age-related macular degeneration using polarization-sensitive optical coherence tomography. Invest Ophthalmol Vis Sci 2010;51:2149-57.
5. Baumann B, Gotzinger E, Pircher M, Sattmann H, Schuutze C, Schlanitz F, Ahlers C, Schmidt-Erfurth U, Hitzenberger CK. Segmentation and quantification of retinal lesions in age-related macular degeneration using polarization-sensitive optical coherence tomography. J Biomed Opt 2010;15:061704.
6. Huang D, Swanson EA, Lin CP, Schuman JS, Stinson WG, Chang W, Hee MR, Flotte T, Gregory K, Puliafito CA, Fujimoto JG, Lin CP, Schuman JS, Puliafito CA. Optical Coherence Tomography. Science, 1991;254:1178-81.
7. Hee MR, Izatt JA, Swanson EA, Huang D, Schuman JS, Lin CP, Puliafito CA, Fujimoto JG. Optical Coherence Tomography of the Human Retina. Arch Ophthalmol 1995;113:325-32.
8. Drexler W, Fujimoto JG. State-of-the-art retinal optical coherence tomography. Prog Retin Eye Res 2008;27:45-88.
9. Zhang A, Zhang Q, Chen CL, Wang RK. Methods and algorithms for optical coherence tomography-based angiography: a review and comparison. J Biomed Opt 2015;20:100901.
10. Gorczynska I, Migacz JV, Zawadzki RJ, Capps AG, Werner JS. Comparison of amplitude-decorrelation, speckle-variance and phase-variance OCT angiography methods for imaging the human retina and choroid. Biomed Opt Express 2016;7:911-42.
11. Jia Y, Tan O, Tokayer J, Potsaid B, Wang Y, Liu JJ, Kraus MF, Subhash H, Fujimoto JG, Hornegger J, Huang D. Split-spectrum amplitude-decorrelation angiography with optical coherence tomography. Opt Express 2012;20:4710-25.
12. Kim DY, Fingler J, Zawadzki RJ, Park SS, Morse LS, Schwartz DM, Fraser SE, Werner JS. Optical imaging of the chorioretinal vasculature in the living human eye. Proc Natl Acad Sci 2013;110:14354-9.
13. Choi W, Mohler KJ, Potsaid B, Lu CD, Liu JJ, Jayaraman V, Cable AE, Duker JS, Huber R, Fujimoto JG. Choriocapillaris and choroidal microvasculature imaging

with ultrahigh speed OCT angiography. PLoS One 2013;8:e81499.

14. Schwartz DM, Fingler J, Kim DY, Zawadzki RJ, Morse LS, Park SS, Fraser SE, Werner JS. Phase-variance optical coherence tomography: A technique for noninvasive angiography. Ophthalmology 2014;121:180-7.

15. Heisler M, Lee S, Mammo Z, Jian Y, Ju M, Merkur A, Navajas E, Balaratnasingam C, Beg MF, Sarunic M V. Strip-based registration of serially acquired optical coherence tomography angiography. J Biomed Opt 2017;22:36007.

16. Ju MJ, Heisler M, Wahl D, Jian Y, Sarunic M V. Multiscale sensorless adaptive optics OCT angiography system for in vivo human retinal imaging. J Biomed Opt 2017;22:1-10.

17. de Boer JF, Hitzenberger CK, Yasuno Y. Polarization sensitive optical coherence tomography - a review [Invited]. Biomed Opt Express 2017;8:1838-73.

18. Makita S, Mino T, Yamaguchi T, Miura M, Azuma S, Yasuno Y. Clinical prototype of pigment and flow imaging optical coherence tomography for posterior eye investigation. Biomed Opt Express 2018;9:4372-89.

19. Ju MJ, Hong YJ, Makita S, Lim Y, Kurokawa K, Duan L, Miura M, Tang S, Yasuno Y. Advanced multi-contrast Jones matrix optical coherence tomography for Doppler and polarization sensitive imaging. Opt Express 2013;21:19412.

20. Makita S, Hong YJ, Miura M, Yasuno Y. Degree of polarization uniformity with high noise immunity using polarization-sensitive optical coherence tomography. Opt Lett 2014;39:6783.

21. Jian Y, Lee S, Ju MJ, Heisler M, Ding W, Zawadzki RJ, Bonora S, Sarunic M V. Lens-based wavefront sensorless adaptive optics swept source OCT. Sci Rep 2016;6:27620.

22. Bonora S, Jian Y, Zhang P, Zam A, Pugh EN, Zawadzki RJ, Sarunic M V. Wavefront correction and high-resolution in vivo OCT imaging with an objective integrated multi-actuator adaptive lens. Opt Express 2015;23:21931.

23. Verstraete HRGW, Heisler M, Ju MJ, Wahl D, Bliek L, Kalkman J, Bonora S, Jian Y, Verhaegen M, Sarunic M V. Wavefront sensorless adaptive optics OCT with the DONE algorithm for in vivo human retinal imaging [Invited]. Biomed Opt Express 2017;8:2261.

24. Ju MJ, Heisler M, Athwal A, Sarunic M V., Jian Y. Effective bidirectional scanning pattern for optical coherence tomography angiography. Biomed Opt Express 2018;9:2336-50.

25. Pircher M, Zawadzki RJ. Review of adaptive optics OCT (AO-OCT): principles and applications for retinal imaging [Invited]. Biomed Opt Express 2017;8:2536-62.

26. Liang J, Williams DR. Aberrations and retinal image quality of the normal human eye. J Opt Soc Am A Opt Image Sci Vis 1997;14:2873.

27. Castejón-Mochón JF, López-Gil N, Benito A, Artal P. Ocular wave-front aberration statistics in a normal young population. Vision Res 2002;42:1611-7.

28. Duan L, Hong YJ, Yasuno Y. Automated segmentation and characterization of choroidal vessels in high-penetration optical coherence tomography. Opt Express 2013;21:15787-808.

29. Jian Y, Wong K, Sarunic MV. Graphics processing unit accelerated optical coherence tomography processing at megahertz axial scan rate and high resolution video rate volumetric rendering. J Biomed Opt 2013;18:26002.

30. Xu J, Wong K, Jian Y, Sarunic M V. Real-time acquisition and display of flow contrast using speckle variance optical coherence tomography in a graphics processing unit. J Biomed Opt 2014;19:026001.

31. Xu J, Han S, Balaratnasingam C, Mammo Z, Wong KSK, Lee S, Cua M, Young M, Kirker A, Albiani D, Forooghian F, Mackenzie P, Merkur A, Yu DY, Sarunic M V. Retinal angiography with real-time speckle variance optical coherence tomography. Br J Ophthalmol 2015;99:1315-9.

32. Azuma S, Makita S, Miyazawa A, Ikuno Y, Miura M, Yasuno Y. Pixel-wise segmentation of severely pathologic retinal pigment epithelium and choroidal stroma using multi-contrast Jones matrix optical coherence tomography. Biomed Opt Express 2018;9:2955-73.

33. Liu S, Dzyubachyk O, Eggermont J, Nakatani S, Lelieveldt BPF, Dijkstra J. Histogram-based standardization of intravascular optical coherence tomography images acquired from different imaging systems. Med Phys 2018;45:4158-70.